BIO-INSPIRED CACO$_3$ NANOCOMPOSITE FOR EFFICIENT RADIATIVE COOLING

by

Zixuan Zhao

A Thesis

Submitted to the Faculty of Purdue University

In Partial Fulfillment of the Requirements for the degree of

Master of Science in Mechanical Engineering

School of Mechanical Engineering

West Lafayette, Indiana

May 2019

THE PURDUE UNIVERSITY GRADUATE SCHOOL
STATEMENT OF COMMITTEE APPROVAL

Dr. Xiulin Ruan, Co-Chair

 School of Mechanical Engineering

Dr. Jay Gore, Co-Chair

 School of Mechanical Engineering

Dr. Jong Hyun Choi

 School of Mechanical Engineering

Approved by:

 Dr. Jay Gore

  Head of the Graduate Program

ACKNOWLEDGMENTS

TABLE OF CONTENTS

LIST OF TABLES

LIST OF FIGURES

NOMENCLATURE

d	Particle diameter
f	Particle volume concentration
n	Ratio of particle refractive index to that of matrix
m	Complex refractive index
k	Imaginary part of the complex refractive index
Θ	Angle between directions of propagation and observation
l	Length of the particle
r_{eq}	Equivalent radius
Q	Efficiency
N	Number of particles
a	Radius of the particle
x	Size parameter
λ	Wavelength
n_0	Refraction index of the medium
ε_p	Porosity
ε	Ellipse eccentricity
γ	Length to diameter ratio
σ	Effective scattering coefficient
κ	Effective absorption coefficient
g	Asymmetric parameter
Φ	Scattering phase function
a_n, b_n	Mie coefficients
ψ_n, ξ_n	Riccati-Bessel Functions
π_n, τ_n	Angular scattering patterns

Subscripts

abs	Absorption
sca	Scattering
e	Effective
s	Single
I	Independent
D	Dependent
T	Nanocomposite medium
i	Each particle

ABSTRACT

Author: Zhao, Zixuan. MSME
Institution: Purdue University
Degree Received: May 2019
Title: Bio-Inspired $CaCO_3$ Composite for Effective Radiative Cooling
Committee Chair: Xiulin, Ruan and Jay, Gore

Passive radiative cooling favors the transfer of energy to the deep space (2.7K) by emitting in the transparent atmosphere region (8-13μm) and reflecting incoming solar irradiation. To achieve desired daytime or night time cooling performance, scientists have explored various fine-tuned photonic material combinations and layering techniques. However, the high cost, UV absorption or telecommunication interferences due to the metallic material used. Scalable and low-cost nonmetal materials have been studied, but the absorption in the UV range still remains a limitation. Single crystal $CaCO_3$ was found to be highly reflective in the UV range, but it has not been explored for radiative cooling applications yet. In this work we first studied the reflectance in the solar range of seashells of multi-millimeters thick, and found over 70% reflectance. Inspired by this promising result, we fabricated a bio-inspired material — $CaCO_3$ acrylic nanocomposite, and optimized the nanoparticle size to most strongly reflect the sunlight. We analyzed its performance using Mie Theory and Monte Carlo Simulation for multiple size distribution with dependent scattering correction. The results are in excellent agreement with the experimental data. With 60% volume concentration, the simulation results showed that the total solar reflectance of $CaCO_3$ can achieve up to 97% . Insights obtained from this work will aid researchers in selecting economical, scalable, and manufacturable materials for radiative cooling applications.

1. INTRODUCTION

In 2014, two thirds of the U.S homes have air conditioners, and on average 6% of the total energy was contributed to space cooling for each household, spending 29 billion U.S dollars towards their electricity bill. More importantly, the power usage generated 117 million metric tons of CO_2, exacerbating global warming[1]. In addition, with the development technology in telecommunication, cell phone base station antennas and outdoor devices that require intense power supplies need better cooling solutions without interference with the telecommunication signals. Passive radiative cooling has been a promising solution because of it economical and sustainable advantages. Passive radiative cooling favors the transfer of energy to the deep space (2.7K) [2] by emitting in the transparent atmosphere region (8-13μm) [3]–[10], and reflecting incoming solar irradiation. To achieve desired daytime or night time cooling performance, scientists have explored various fine-tuned photonic material combinations and layering techniques [10]–[16]. Utilizing metallic materials, such as silver, is common to reflect solar irradiation, but may introduce inferences with telecommunication [17], [18]. Metal materials are also expensive [14] when it comes to large volume production. Compared to using metals, nanocomposites with TiO_2 are widely used by many researchers because of its economical fabrication advantages [16], [17], [19]–[22]. However, TiO_2 can absorb approximately 3% of the total solar intensity due to strong absorption in the UV range. HfO_2 was proposed because of its low UV absorption, but relatively expensive [11]. Particles with low-index particles such as SiO_2 are also explored[10], [14], but these attempts have not demonstrated full daytime radiative cooling.

To overcome these obstacles, we started exploring potential material options from the nature and found that there are a large number of snails found in various desserts, and they can survive in environment up to 50 degrees Celsius[24]. Besides the effect of air insulation and its shell structure, one of the main factors that contributes to keeping snails cool in the desert is the effective light reflectance of its shell. Similar to snail shells but more accessible, seashells are also expected to show high reflectance because of the main component, Calcite, $CaCO_3$ [25], [26]. Inspired by the unique thermal advantage of seashells, this study 1) analyzed the optical properties of the shells, 2) synthesized a coating that strengthen the characteristics of seashells using $CaCO_3$ to achieve desired cooling performance in high temperature operating conditions and 3) developed a tool with Mie theory and Monte Carlo Simulation to explain the reflectance of the nanocomposite computationally. Insights obtained from this study will aid researchers in selecting economical, scalable, and manufacturable materials for radiative cooling applications. The author hypothesizes that:

1) Compared to a single particle, multiple size particle distribution may help increase the reflectance of a nanocomposite because particles with different sizes can scatter at different solar wavelength, thus enhance the total solar reflectance.

2) For closed packed particles, incorporating dependent scattering may improve the reflectance.

2. LITERATURE REVIEW

2.1 Passive Radiative Cooling and Current State of Art

Passive radiative cooling favors the transfer of energy to the deep space (2.7K) [2] by emitting in the transparent atmosphere region (8-13μm) [3]–[10], and reflecting incoming solar irradiation. For an ideal emitter in the sky window approximately the threshold of the total solar reflectance to achieve daytime radiative cooling is 85%. Every 1% of the improvement of reflection will increase the cooling power by $10 W/m^2$ [17]. To achieve desired daytime or night time cooling performance, scientists have explored various fine-tuned photonic material combinations and layering techniques [10]–[16]. Typically, the top layers demonstrate high emissivity to the sky. The bottom layers tend to show high reflectivity in the solar range. Utilizing metallic materials, such as silver at the bottom layer, is common to reflect solar irradiation, but may introduce inferences with telecommunication [17], [18]. Metal materials are also often expensive [14] when it comes to large volume production. Compared to using metals, nanocomposites with TiO_2 are widely used by many researchers because of its economical fabrication advantages [16], [17], [19]–[22]. However, TiO_2 can absorb approximately 3% of the total solar intensity in the UV range due to high absorption in the UV range [23]. HfO_2 was proposed because of its low UV absorption, but relatively expensive [11]. Particles with low-index particles such as SiO_2 are also explored[10], [14], but these attempts have not demonstrated daytime radiative cooling yet. In addition, elastomer-based materials [14] could be an alternative to ensure the reliability of the coating. The following table has summarized the explorations of research mentioned above.

Table 2.1 Summary of various radiative cooling coating development

Author (s)	Materials/Techniques	Results	Disadvantages
Huang and Ruan [16]	Top layer: TiO_2 acrylic nanocomposite Bottom layer: carbon black paint	A daytime net cooling power $\sim 100\ \frac{W}{m^2}$, $180\ \frac{W}{m^2}$ for nighttime	TiO_2 UV absorption
Raman et al [11].	Top layers: seven layers of HfO_2 and SiO_2 Bottom layers: Ag +Ti adhesion layer +Si wafer substrate	First demonstrated day time cooling Cooling surface ~5 °C below the ambient air temperature under direct sunlight. Reflecting 97 % of incident sunlight high emittance in "sky window" Cooling power 40.1 $\frac{W}{m^2}$	Silver (expensive) Not scalable
Gentle et al.[13]	Top layer: Specifically engineered polyesters Bottom layer: silver thin film	Cooling surface ~11 °C compared to the roof nearby. Showing ~ 100 % for both solar reflectance and thermal emittance in "sky window"	Silver (expensive)
Zhai et al [10].	Top layer: 6% by volume resonant polar dielectric SiO_2 microspheres randomly distributed in a polymethylpentene (TPX) matrix Bottom layer: 200nm-thick silver coating	Manufacturable Emissivity>0.93 across the atmosphere transmission window and reflect 96% solar irradiation $93\ \frac{W}{m^2}$ cooling power under direct sunlight	Outdoor reliability of glass-polymer hybrid metamaterials is not validated Silver (expensive)
Kou et al [15]	Top layer: fused silica wafer and polydimethylsiloxane (PDMS) film Bottom layer: silver film back reflector	$\sim 127\ \frac{W}{m^2}$ cooling power during daytime	Absorption in the ultraviolet need to be decreased Silver expensive
Atiganyanun et. Al [14].	Randomly packed SiO_2 microspheres	Cooling a black surface ~ 12 °C under sunlight.	Lack of reliability testing

Table 2.1 continued

Li et al [27]	BaSO$_4$ film CaCO$_3$-acrylic paint TiO$_2$-acrylic paint	$\sim 110 \frac{W}{m^2}$ cooling power when the average solar irradiation is $930 \frac{W}{m^2}$ Cooling a surface ~ 4.5 °C below the ambient temperature at noon	Experimental results only

2.2 Radiative Cooling in Bio-Systems

When challenges cannot be solved, inspirations and solutions can come from the nature. Saharan silver ants can survive one of the hottest place on earth [28], because they form a dense array of triangular hairs on their skin surface. The hair structure enhances the reflectivity in the visible and near-infrared range through Mie scattering and total reflection [29], as seen in Figure 2.1.
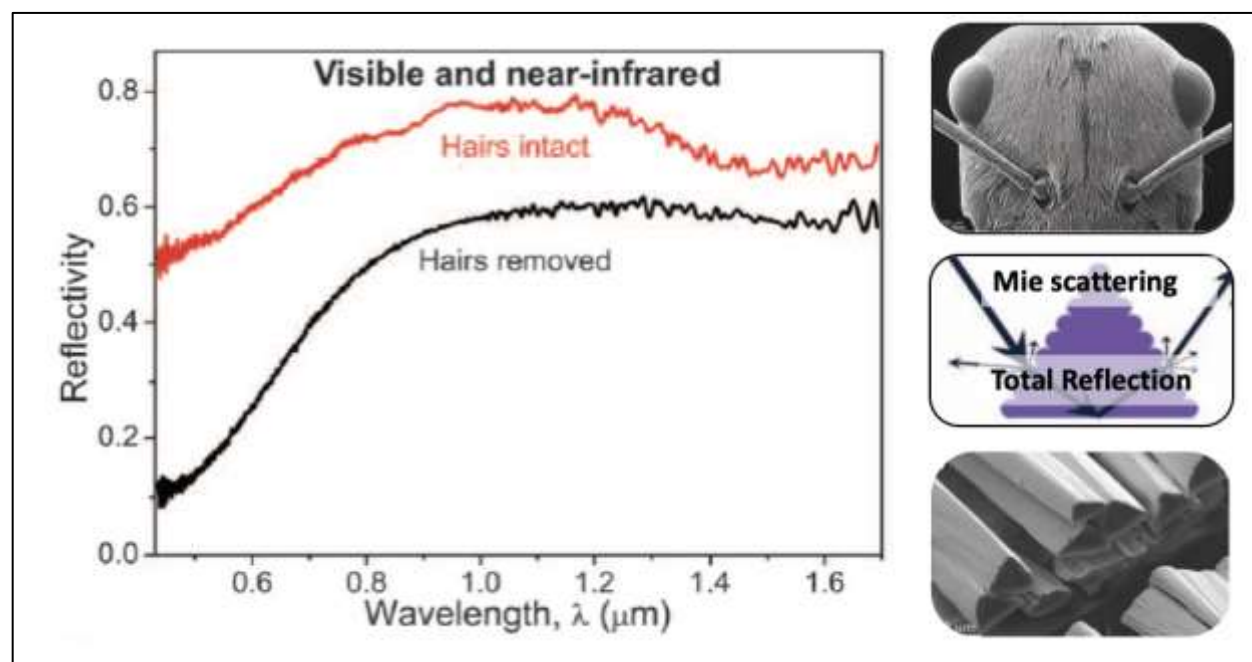
Figure 2.1 Triangular hairs enhance reflectivity in the visible and NIR by Mie scattering and total reflection [29]

Inspired by how Saharan silver ants adapt the nature, our research group started looking into similar environments where certain animals can keep themselves cool under high temperature. It was found a large number of snails can survive in environments up to 50 degrees Celsius in various desserts [24]. Besides the effect of air insulation and its shell structure, the main factor that contributes to keeping snails cool in the desert is the light reflectance by their white shells, which are composed of $CaCO_3$. A spectrometry study was conducted by the United States Geological Survey (USGS) for $CaCO_3$ pure single crystal and the average grain size is $410 \, \mu m$ [30]. As shown in Figure 2.2, $CaCO_3$ demonstrates a very promising reflectance in the ultraviolet (UV) and visible range. Even though there are optical properties measured, however, no research has investigated how $CaCO_3$ can be utilized in radiative cooling applications. Challenges include how to make the materials easy to use and how to reduce the thickness needed. We were motivated to develop a scalable, cost effective paint that demonstrates high solar reflectance and high sky-window emittance using $CaCO_3$ nanocomposite.
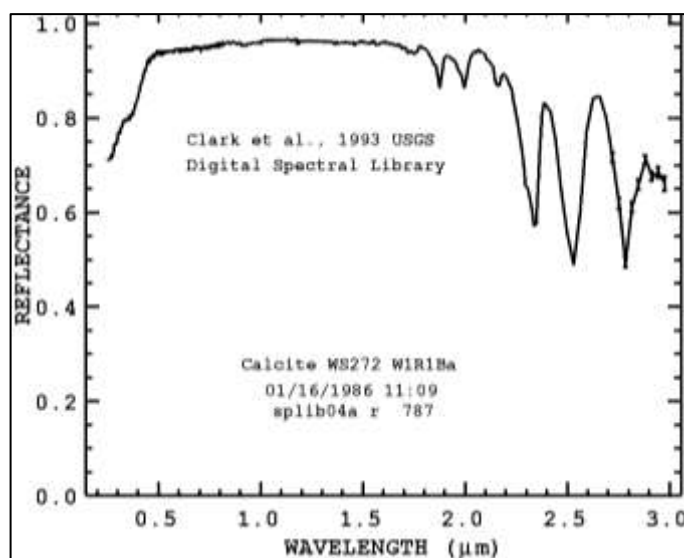
Figure 2.2 Reflectance of single crystal calcite in the solar spectrum [30]

3. BIO INSPIRED SYSTEMS

3.1 Seashell Characterization

Like mentioned before, snail shells demonstrated its high reflectance and can keep snails cool in the desert. However, snail shells are not readily available. An alternative was found to be seashells, which also appear to be white and are more accessible. Since Calcite ($CaCO_3$) is a major component in seashells [25], [26], it is also expected to demonstrate high reflectance in the solar spectrum. Therefore, the reflection, transmission and absorption were measured first for natural seashell to study the potential performance of $CaCO_3$ (Table 3.1). As shown in Figure 3.1, the small semi-transparent seashell demonstrated 53% total reflection, whereas thick opaque seashell showed 76% total reflection. This thickness-trend is consistent with previous measurements on bulk calcite where the reflectance is very high. In addition, it was found that the bandgap of $CaCO_3$ also supports its performance. The bandgap of a material illustrates the segment of the solar spectrum a material can absorb [31]. When a material is associated with a low bandgap, such as TiO_2, with 3.2eV, it tends to introduce absorptivity in the UV range. However, compared to TiO_2, the bandgap of $CaCO_3$ is approximately 6eV [32], providing low absorptivity in the UV range. These results not only illustrated that $CaCO_3$ could be a promising material for radiative cooling purposes, they also encourage the author to develop solutions with $CaCO_3$ nanocomposite to outperform natural seashells. In developing our paints, we need to achieve higher reflectance with a smaller thickness, which are not trivial to achieve.
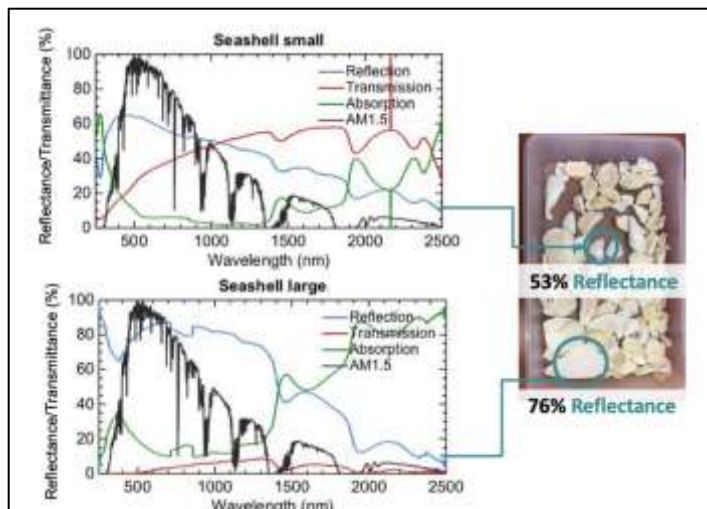
Figure 3.1 Natural seashell reflection, transmission and absorption 0-2500nm

Table 3.1 Reflection, transmission and absorption of seashells

	Small Seashell	Large Seashell
Reflection	0.535	0.757
Transmission	0.382	0.033
Absorption	0.083	0.210

4. RADIATIVE COOLING PAINT

4.1 Fabrication of Radiative Cooling Paint

In order to achieve high solar reflectance with a relatively small thickness, we optimized the nanoparticles size to most strongly scatter the solar spectrum , and used very high concentration. 60 % volume concentration of $CaCO_3$ particles are utilized with 1.9 μm particle size reported by the manufacturer (Atlantic Equipment Engineers). Acrylic resin is used as the embedding matrix due to its common usage in the paint industry. In addition, for materials that do not exhibit phonon-polariton resonance in the sky window, the matrix itself need to emits in the sky window to provide cooling power and acrylic is a low-cost matrix that emits in the sky window.

The following steps are conducted during the sample preparation:

1) Mix acrylic resin (A) and $CaCO_3$ particles (B to achieve a consistent form (C)

2) Place the sample on the hot plate with a stir bar (D) to ensure uniform particle distribution

3) Apply the paint onto a surface to form a film (E)
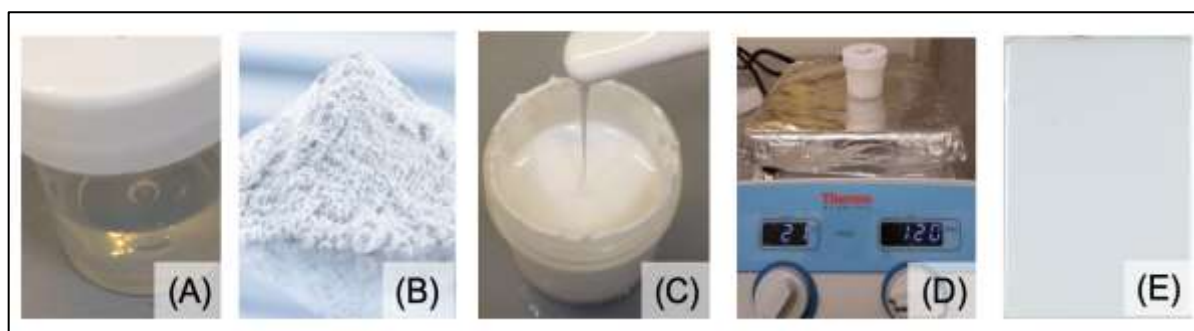
Figure 4.1 Sample Fabrication Process

The samples are measured by a PerkinElmer Lambda 950 spectrometer with a built-in integrating sphere. The wavelength ranges from 250 nm to 1100 nm. A schematic of the experimental setup

can be seen in Figure 4.2. Hitachi S-4800 Scanning Electron Microscope (SEM) (Figure 4.3) was used to study the optical and morphological characteristics of $CaCO_3$ samples.
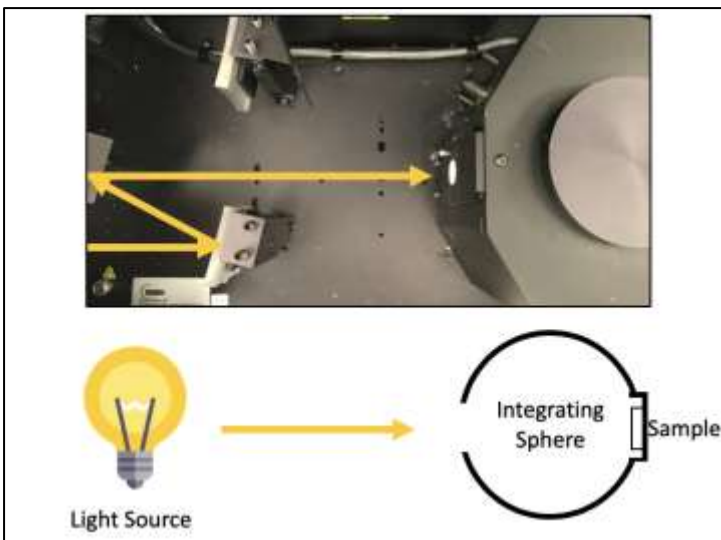
Figure 4.2 Experimental set up for optical measurements

Figure 4.3 Hitachi S-4800 Scanning Electron Microscope

4.2   Experimental Results

After the fabrication process, the sample was placed on the spectrometer for optical property measurement. Figure 4.4 shows the reflectance of the 1.9μm $CaCO_3$-acrylic composite paint with 60% volume concentration. The sample has a total reflection of 95.1% [27].
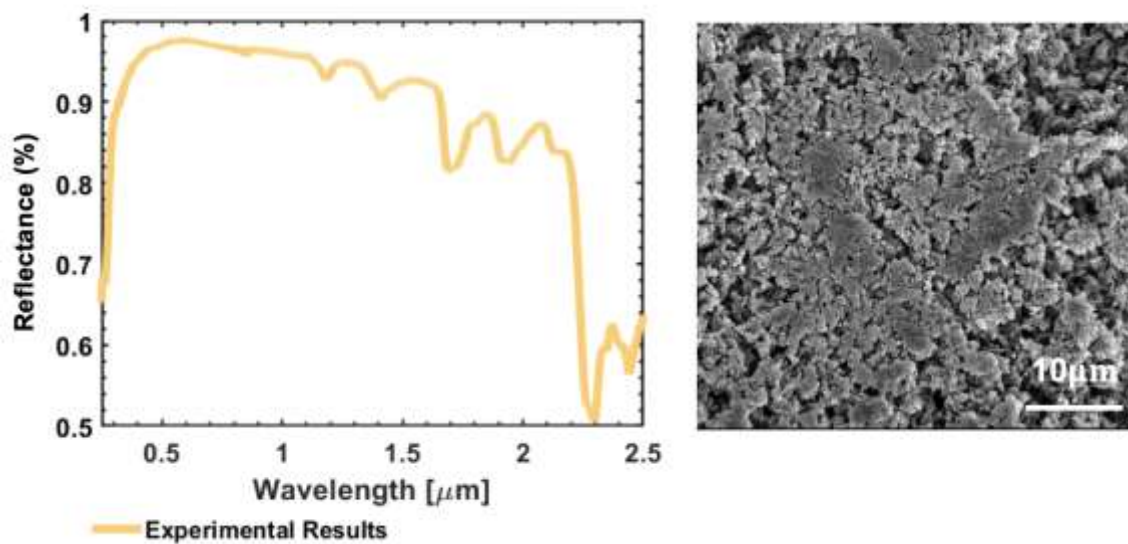
Figure 4.4 Reflectance of CaCOɜ-acrylic composite paint
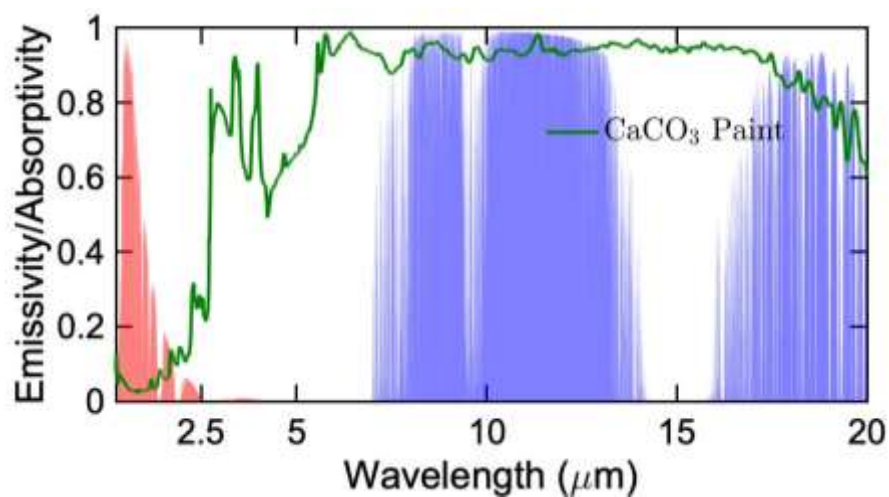
Figure 4.5 Emissivity of CaCOɜ-acrylic composite paint

In addition to high reflectance in the solar spectrum, high emissivity in the sky-window is another criterion for effective radiative cooling. Therefore, the emissivity of the sample was also measured, as seen in Figure 4.5 [27]. The sample indicates high emissivity in the "sky window" .
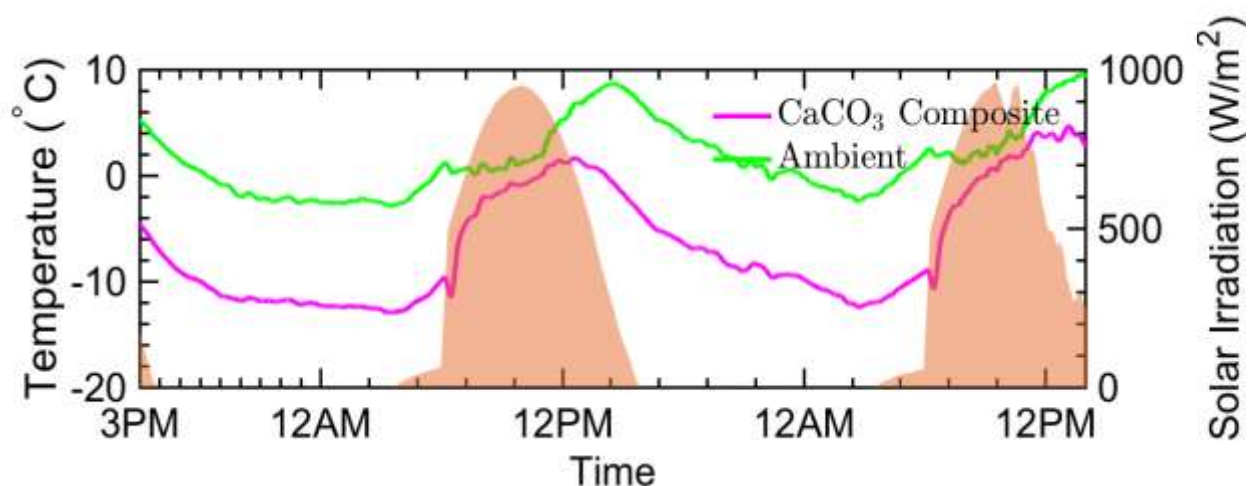
Figure 4.6 Outdoor temperature measurements for CaCOз-acrylic composite paint over 24 hours. The orange region represents for solar irradiation intensity.
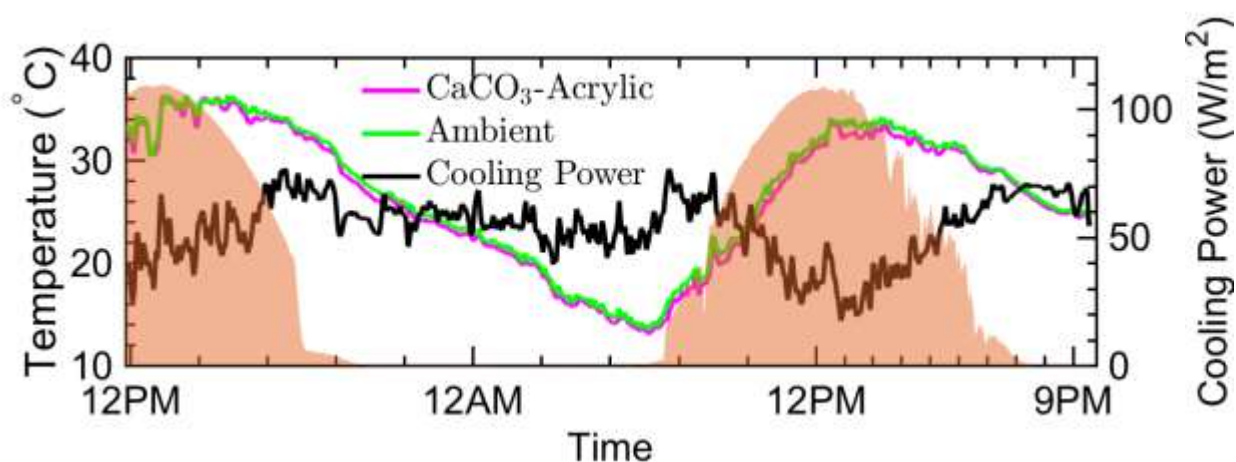
Figure 4.7 Direct measurements of the cooling power for CaCOз-acrylic composite paint using a feedback heater. The orange region represents solar irradiation intensity.

Outdoor data was collected in West Lafayette to illustrate the full day-time cooling. The sample was able to maintain 1.7 °C below the ambient temperature when the peak solar irradiation reaches $950 W/m^2$ during the day. The average cooling power is approximately $37 W/m^2$ and $56 W/m^2$ for night time and day-time respectively [27].

5. SIMULATIONS

Having a computational model can help predict the reflectance of materials and generate important insights. However, studying reflectance of nanoparticle composites can be computationally challenging when solving Maxwell equations even though it provides high accuracy. Direct Monte Carlo method offers an alternative by recording each photon's location and tracking the trajectory, but with the number of particles, this method can be unrealistic. This work adopts the methods used by Peoples et al [17], where Mie theory, effective medium and Monte Carlo method are utilized collectively. Mie theory was used to study the property of a single particle, including its scattering coefficient, absorption coefficient and phase function. Since the nanocomposite is assumed to be an effective medium, the volume-averaged coefficients are applied to predict the behavior of the entire nanocomposite. Monte Carlo method ultimately solves the radiative transfer equation stochastically to determine the reflectance, transmission and absorption of the nanocomposite. This section will 1) demonstrate the implementation of Mie Theory in the simulation and 2) illustrate the use of Monte Carlo in the computational model.

5.1 Mie Theory Simulation

Mie scattering occurs when the particle size is comparable to the wavelength of the incoming light[33]. This work utilized the computational model proposed by Peoples et al [17] to calculate the scattering and absorption coefficient for multiple particles sizes, similar to the approach presented by Huang and Ruan for single particle size [16]. The open source Monte Carlo code was first developed by Matzler [34].

The following assumptions are made in our Mie Theory Simulation :

- Matrix absorption is neglected [17], [35], [36],

- The refractive index of a particle is divided by the refractive index of the medium n_o [37]–[39].

- Photons move randomly and independent of each other

The Mie Theory simulation model requires two inputs: 1) the size parameter x and 2) the complex refractive index m. The following steps are used for the Mie Theory Simulation

Step 1: Find Mie Coefficient Calculation

$$a_n = \frac{m\psi_n(mx)\psi_n'(x) - \psi_n(x)\psi_n'(mx)}{m\psi_n(mx)\xi_n'(x) - \xi_n(x)\psi_n'(mx)} \qquad (5.1)$$

$$b_n = \frac{\psi_n(mx)\psi_n'(x) - m\psi_n(x)\psi_n'(mx)}{\psi_n(mx)\xi_n'(x) - m\xi_n(x)\psi_n'(mx)} \qquad (5.2)$$

Where ψ_n and ξ_n are the Riccati-Bessel Functions given by:

$$\psi_n(r) = rj_n(r) \qquad (5.3)$$

$$\xi_n(r) = rh_n^{(1)}(r) \qquad (5.4)$$

the subscript "n" denotes the order of Bessel function. For Mie Scattering a numerical approximation for convergence is given to be:

$$n_{max} = x + 4x^{1/3} + 2 \qquad (5.5)$$

Step 2: Find Scattering, Extinction, and Absorption efficiencies and Asymmetric parameter:

$$Q_{sca} = \frac{2}{x^2} \sum_{n=1}^{n_{max}} (2n+1)(|a_n|^2 + |b_n|^2) \qquad (5.6)$$

$$Q_{ext} = \frac{2}{x^2} \sum_{n=1}^{n_{max}} (2n+1)Re(a_n + b_n) \qquad (5.7)$$

$$Q_{abs} = Q_{ext} - Q_{sca} \qquad (5.8)$$

The output of Mie Theory calculation is the asymmetric parameter for a single particle, which will be used as the input for the Monte Carlo simulation in the next section. The asymmetry parameter is the average cosine [37]of the scattering which depends on the polarization stage of the incident light. However, if the particle is a sphere, then it is independent of the polarization [37] The asymmetric parameter for a single particle is expressed as [16],

$$g_s = Q_{sca} < cos\theta > \qquad (5.9)$$

$$= \frac{4}{x^2} [\sum_{n=1}^{\infty} \frac{n(n+2)}{n+1} Re(a_n a_{n+1}^* + b_n b_{n+1}^*) + \sum_{n=1}^{\infty} \frac{2n+1}{n(n+1)} Re(a_n b_n^*)]$$

Where x is the size parameter, a_n and b_n are the Mie coefficients [16], [37], [40]and the a_n^* and b_n^* are conjugate transpose of a_n and b_n respectively.

Step 3: Find Scattering and Absorption Coefficient for single size parameters:

$$\sigma_{s\lambda} = \frac{\pi d^2}{4} f Q_{sca} \qquad (5.10)$$

$$\kappa_\lambda = \frac{\pi d^2}{4} f Q_{abs} \qquad (5.11)$$

Step 4: Find Scattering Amplitudes:

$$S_1(cos\theta) = \sum_{n=1}^{n_{max}} \frac{(2n+1)}{n(n+1)} (a_n \pi_n + b_n \tau_n) \qquad (5.12)$$

$$S_2(cos\theta) = \sum_{n=1}^{n_{max}} \frac{(2n+1)}{n(n+1)} (a_n \tau_n + b_n \pi_n) \qquad (5.13)$$

Where π_n and τ_n describe angular scattering patterns and are related to the Legendre Polynomials by:

$$\pi_n(cos\theta) = \frac{dP_n(cos\theta)}{dcos(\theta)} \qquad (5.14)$$

$$\tau_n(cos\theta) = cos\theta\,\pi_n(cos\theta) - sin^2\theta\,\frac{d\pi_n(cos\theta)}{dcos(\theta)} \qquad (5.15)$$

Step 5: Find Scattering Phase Function:

$$\Phi(\theta) = 2\frac{|S_1|^2 + |S_2|^2}{x^2 Q_{sca}} \qquad (5.16)$$

5.2 Monte Carlo Simulation

In the Monte Carlo simulation, the photons are assumed to be independently scattered and the domain is assumed to be semi-infinite in XY-Plane, but finite Z. This method stochastically solves the Radiative Transfer Equation:

$$\frac{dI_\lambda}{ds} = \kappa_\lambda I_{\lambda b} - (\kappa_\lambda + \sigma_{\lambda s})\,I_\lambda + \frac{\sigma_{\lambda s}}{4\pi}\int_{4\pi} I_\lambda(\hat{s}_i)\,\Phi_\lambda(\hat{s}_i, \hat{s})d\Omega_i \qquad (5.17)$$

There is a well-established open source code developed by Wang et al. to simulate the photon transport in multi-layer tissues [41]. The simulation examines randomized events to predict the occurrence the events of interest by ray tracing each photon. It has been adopted by many researchers to tackle radiative heat transfer problems [16], [40], [42], [43]. In a typical calculation, 1,000,000 photons were inserted per wavelength for 59 discrete wavelengths. An initial asymmetry parameter is required from the Mie Theory Simulation to initiate the Monte Carlo calculation. Once the asymmetric parameter is entered, the simulation will solve the Radiative Transfer Equation to establish the reflectance, transmittance and absorption of the nanocomposite.

5.3   Effect of Particle Size Distribution

5.3.1   Single Particle Size Assuming Perfect Spheres with Independent Scattering

Reflectance results were first obtained using averaged single particle size. The average size of each

$CaCO_3$ particle is determined by analyzing 89 points from the SEM images shown in Figure 5.1.
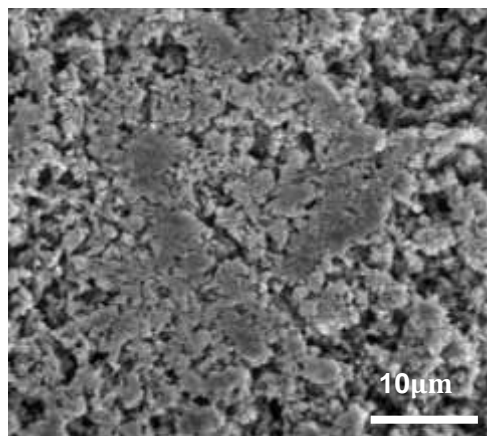
Figure 5.1 SEM of CaCO₃ with 10 K
Magnification

The average radius was found to be 0.57μm and then is used as an input for Mie Theory calculation.

According to Figure 5.2, the predicted reflectance is 73%, as seen in Table 5.1, and is relatively

low compared to the experimental reflectance of 95.1% with the same concentration, thickness

and particle size [27]. A breakdown of reflection in the UV, VIS and NIR ranges can be found in

Appendix Table B.1.
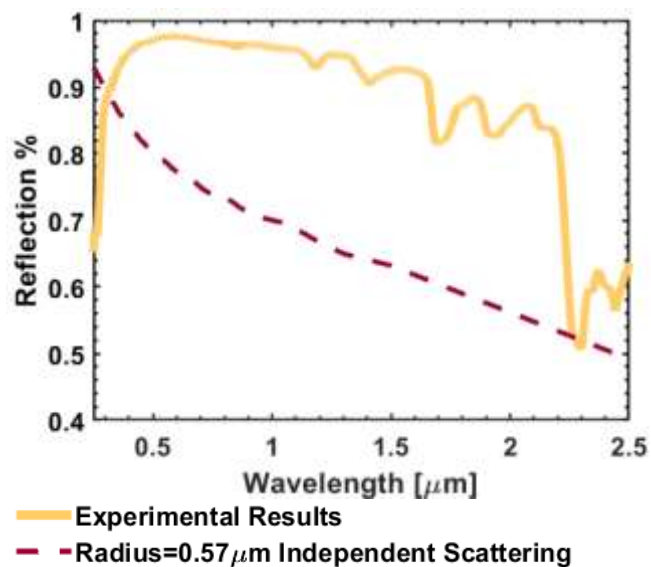
Figure 5.2 Reflection of CaCO₃ nanocomposite to study the effect of single particle size assuming spheres with independent scattering

Table 5.1 Total reflection of CaCO₃ nanocomposite in solar range for a single particle (R=0.57μm)

Model	Total Solar Reflectance [%]
Experimental (⎯⎯)	95.1
Simulation (‒ ‒) R=0.57μm	73.3

5.3.2 Single Particle Size Assuming Ellipsoids with Independent Scattering

To address the discrepancy found in the first attempt, high definition SEM images with magnification of 30,000 were analyzed as shown in Figure 5.3. Additional SEM images analyzed can be found in Appendix A.
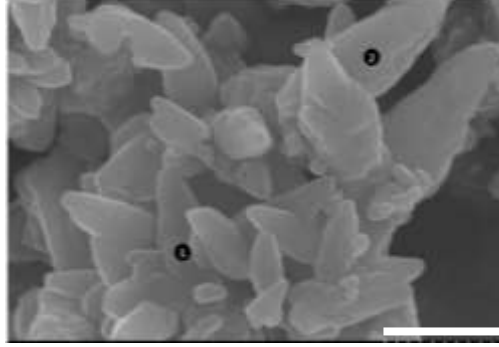
Figure 5.3 SEM of CaCO₃ with 30 K
Magnification

Since acrylic was causing charging issues, it was hard to identify CaCO₃ particles in the nanocomposite. Therefore, instead of examining the nanocomposite as a whole, only CaCO₃ particles were analyzed under SEM. It was surprising that the CaCO₃ particles are not perfect spheres, rather, they are ellipsoids. To account for the irregularity of the geometry, equivalent radius was implemented for CaCO₃ particles as if they were spheres. The following equations [44] are used to calculate the equivalent radius of the CaCO₃ particles.

$$ r_{eq} = \frac{l\varepsilon}{\varepsilon + \gamma \sin^{-1}\varepsilon} \tag{5.18} $$

Where $\varepsilon = \sqrt{1 - \frac{1}{\gamma^2}}$ is the ellipse eccentricity, γ is the length to diameter ratio, l is the length of the particle.

10 points were utilized to obtain the average size of each $CaCO_3$ particle and the average radius was updated to 0.45μm from the high amplification SEM images. With the implementation of ellipsoid equivalent radius, there is not a significant improvement in reflectance from 0-2.5μm as seen in Figure 5.4. According to Table 5.2, the improvement of total reflectance is less than 1% from 0.57μm to 0.45μm.
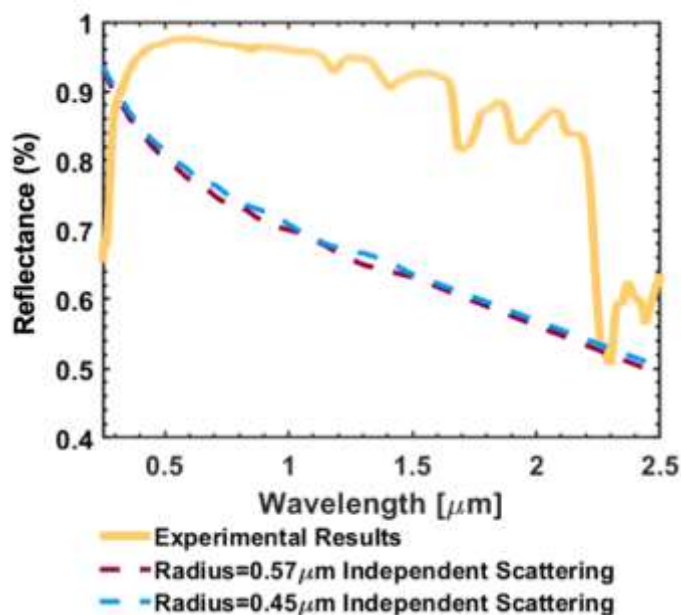
Figure 5.4 Reflection of CaCO₃ nanocomposite (comparison of experimental results, radius=0.57μm and radius=0.45μm indepndent scattering)

Table 5.2 Total reflection of CaCO₃ nanocomposite in solar range for a single particle size(R=0.57μm and R=0.45μm)

Model	Total Solar Reflectance [%]
Experimental (———)	95.1
Simulation (— -) $R=0.57\mu m$	73.3
Simulation (— -) $R=0.45\mu m$	74.2

5.3.3   Multiple Particle Sizes Assuming Ellipsoids with Independent Scattering

Inspired by People et al's approach [17] of enhancing the reflectance of TiO_2 with multiple particle size distribution, we attempted to incorporate multiple particle size instead of assuming all the CaCO₃ particles share the same size, where acrylic is approximated as the effective medium.

The scattering coefficient, absorption coefficient, asymmetric parameter and the phase function are modified based on the weighted average of the original values as:

$$\sigma_{s\lambda} = \frac{\pi d^2}{4} f Q_{sca} = \sum_{i=1}^{c} \frac{3\, f_i\, Q_{sca,i}}{2\, d_i} \tag{5.19}$$

$$\kappa_{S\lambda} = \frac{\pi d^2}{4} f Q_{abs} = \sum_{i=1}^{c} \frac{3\, f_i\, Q_{abs,i}}{2\, d_i} \tag{5.20}$$

$$g = Q_{sca} \langle \cos\theta \rangle = \frac{1}{\sigma_{s\lambda}} \sum_{i=1}^{c} \frac{3\, f_i\, g_{s,i}\, Q_{sca,i}}{2\, d_i} \tag{5.21}$$

$$\Phi(\theta) = 2 \frac{|S_1|^2 + |S_2|^2}{x^2 Q_{sca}} = \frac{1}{\sigma_{s\lambda}} \sum_{i=1}^{c} \frac{3\, f_i\, \Phi_{s,i}(r_i, \theta)\, Q_{sca,i}}{2\, d_i} \tag{5.22}$$

With the implementation of multiple particle sizes, the input for Mie Theory simulation requires modification. Instead of averaging the measurements of the particles, additional calculation of the standard deviation is needed in order to generate randomized particle with different sizes. 0.09 was are found to be the standard deviation when the radius is 0.45μm.. The weighted percentages collectively contribute the total the volume concentration in the Mie Theory simulation as illustrated in Table 5.3.

Table 5.3 Weight percentage calcualtion based on size distribution (R=0.45 μm).

Bin #	Overall Percentage	60% Weighted Percentage
1	10%	0.06
2	30%	0.18
3	40%	0.24
4	20%	0.12

As seen in Figure 5.5, compared to single particle size with independent scattering, the reflection of multiple particle size distribution $(0.45 \pm 0.09 \mu m)$ with independent scattering demonstrates

over 30% improvement. Major improvements can be observed from each individual spectrum as well, 14% , 23% and 36% for UV, VIS and NIR respectively (Table B.2). By adding the effects of multiple particle sizes, each particle can scatter at different parts of the solar spectrum, therefore improving the overall reflectance. The absorption results are still close to zero because the multiple size has a negligible impact due to negligible absorption coefficient [45], therefore they are not plotted as it will adds clutter to the figure.
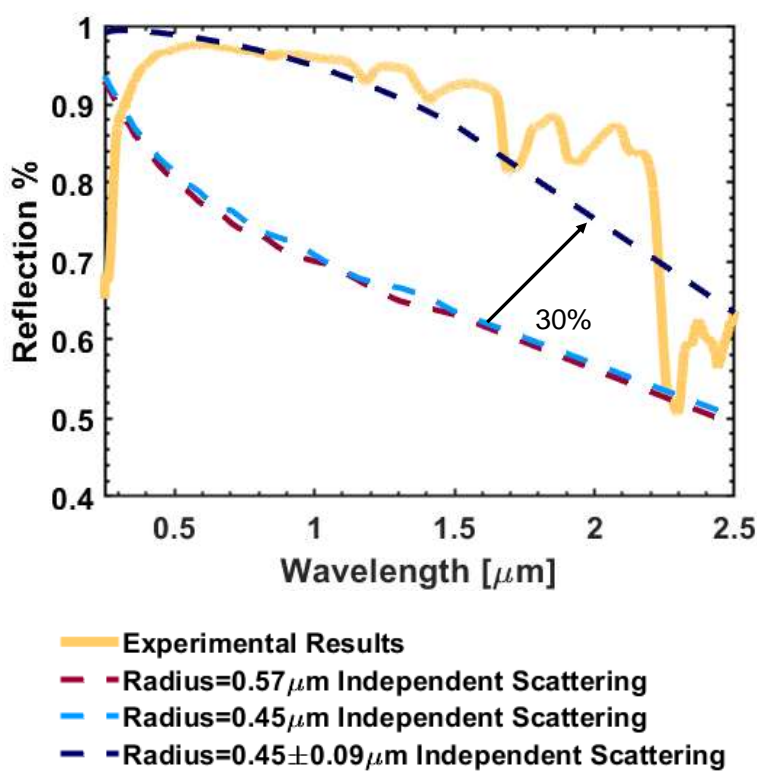
Figure 5.5 Reflection of CaCO₃ nanocomposite to study the effect of multiple particle sizes

Table 5.4 Total reflection of CaCO₃ nanocomposite in solar range for a single particle size (R=0.57μm and R=0.45μm) and mutiple particle sizes (R=0.45μm)

Model	Total Solar Reflectance [%]
Experimental (——)	95.1
Simulation (— -) R=0.57μm	73.3
Simulation (— -) R=0.45μm	74.2
Simulation (— -) R=0.45 ± 0.09 μm	96.3

5.4 Effect of Dependent Scattering

Even though the reflectance has been improved significantly after introducing multiple particle sizes, there is still room for improvement due to the high volume concentration of the nanocomposite because according to Peoples' et al, their strategy only applies to low volume concentrations [17], where a particle in a cloud is not affected by the proximity of its neighboring particles [35]. However, when particles are closely packed together, dependent scattering takes places, where the particle of interest is affected by its surrounding particles.

To better capture the complex interaction among particles, dependent scattering physics need to be incorporated for high volume concentration particles matrix. Although the transition line for dependent and independent scattering is vaguely defined in existing literatures [46] [35], Yamada et al used a 5% deviation from independent Mie theory to define the line where a critical $\frac{c}{\lambda}$ is given as 0.5. Singh and Kaviany [47] proposed a model to analyze dependent scattering using independent properties by scaling the optical thickness. Simpler correcting factors were developed

by Redmond et al [48] to predict dependent scattering coefficient from properties of independent scattering and porosity. We decided to use the following simplified empirical correlation proposed by Redmond et al[48]. The dependent scattering and absorption coefficients are calculated based on the equations below:

$$Q_{sca\_D} = Q_{sca}[1 + 1.5(1 - \varepsilon_p) - 0.75(1 - \varepsilon_p)^2] \tag{5.23}$$

$$Q_{abs\_D} = Q_{abs}[1 + 1.5(1 - \varepsilon_p) - 0.75(1 - \varepsilon_p)^2] \tag{5.24}$$

Where ε_p is the porosity of the matrix.

To compare the effectiveness of the dependent correction factor, both single size and multiple particle size cases were further implemented by applying the correction factor in the Mie Theory simulation, generating the new asymmetric parameters for Monte Carlo simulation. As shown in Figure 5.6, the solid red and blue curves indicate improvements in scattering coefficients when applying the correction factors for both single particle size and multiple particle size. Only scattering properties are plotted due to the small impact of absorption properties for dependent effects and agglomeration[45].
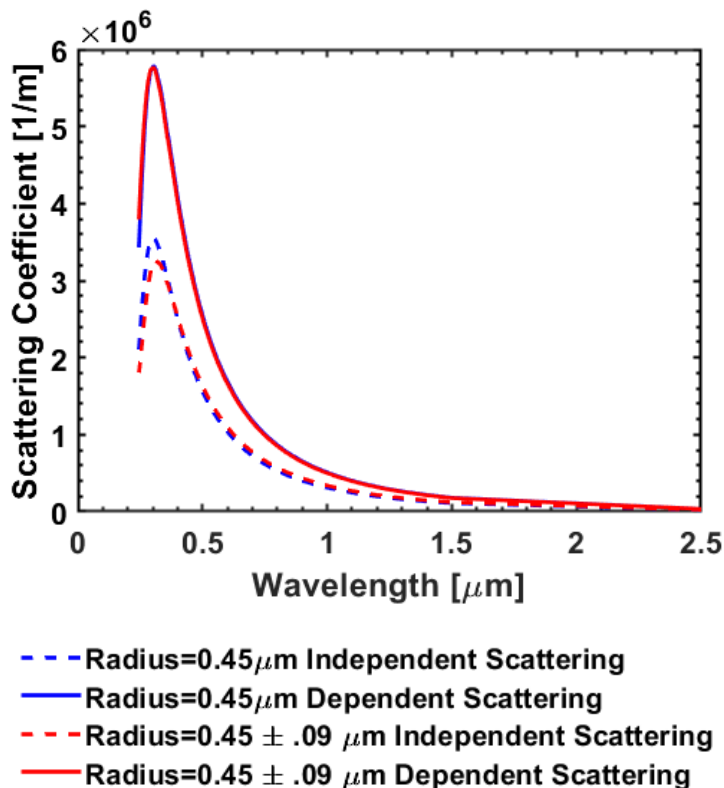
Figure 5.6 Scattering coefficient of CaCO₃ nanocomposite
for a single particle size and multiple particle sizes

As observed in Figure 5.6, the peaks of scattering coefficient are not significantly different when comparing the cases of a single particle size and multiple particle sizes. To isolate the effect of the acrylic matrix, the scattering coefficient of $CaCO_3$ particles for radius ranging from 0.3µm to 0.7 µm was plotted in Figure 5.8. The peaks of the scattering coefficient shifted to higher wavelength when the size increased. When $CaCO_3$ was embedded in the acrylic matrix, the scattering coefficients are diminished after 0.5 µm wavelength as seen in Figure 5.9. This is because the refractive index of the particle is close to that of the matrix as seen in Figure.5.7 and the scattering coefficient will be affected [49]
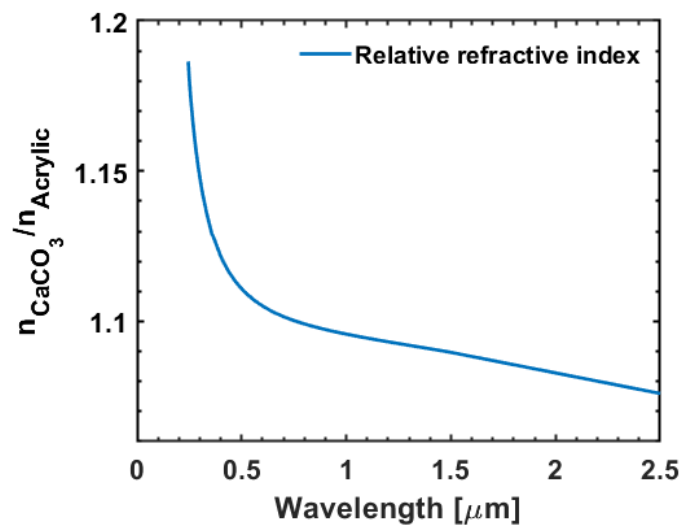
Figure 5.7 Relative refractive index of CaCO₃ particles in acrylic
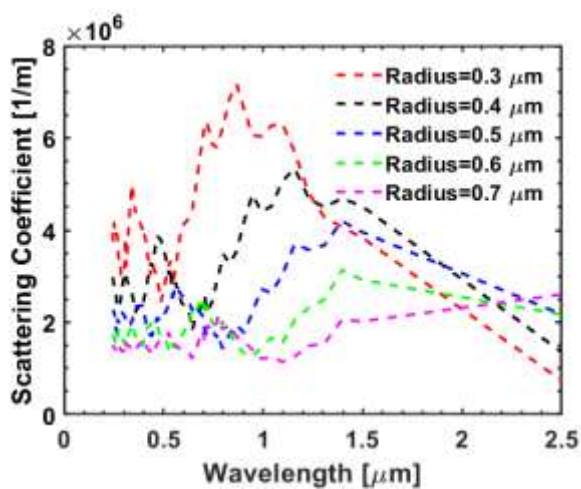
Figure 5.8 Scattering coefficient of CaCO₃ particles in air
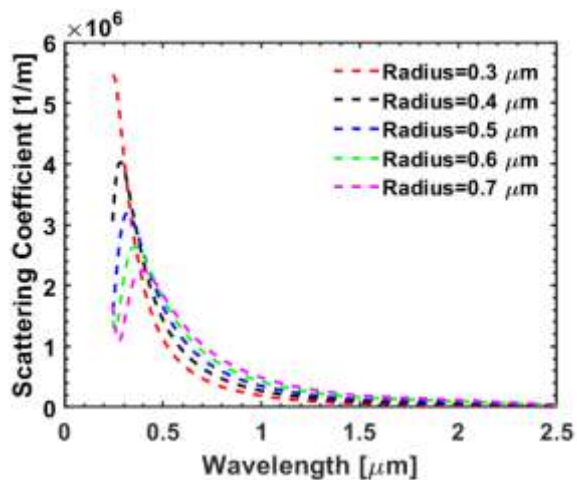
Figure 5.9 Scattering coefficient of CaCO₃ particles in acrylic
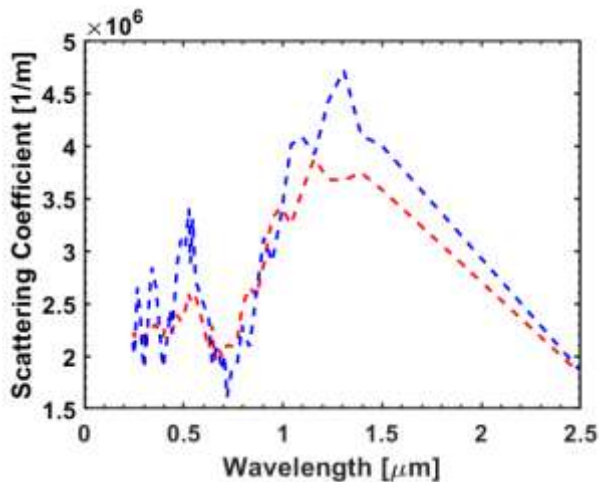
Figure 5.10 Scattering coefficient of CaCO₃ particles in air with a single particle size and multiple particle sizes
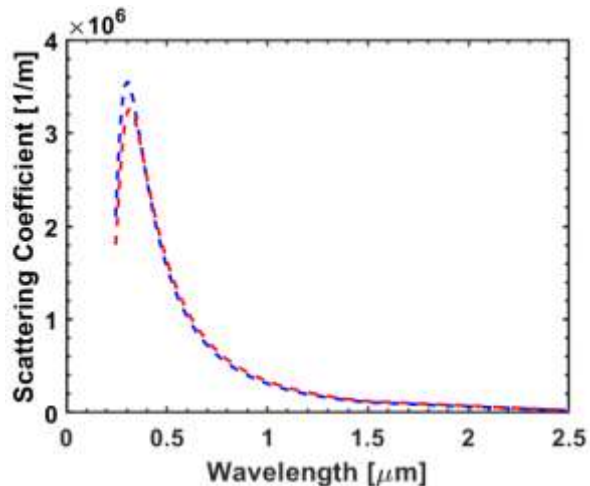
Figure 5.11 Scattering coefficient of CaCO₃ particles in acrylic with a single particle size and multiple particle sizes

According to Figure 5.12, with dependent scattering, the reflection of single particle size increases 10% and for multiple size particle distribution, the reflection increases 1%. The improvement for multiple particle sizes is not as significant as when dependent correct was applied to a single particle size due to the effect of diminishing return. In addition to reflectance, the phase functions at 0.24μm, 0.9μm and 2.5μm of nanocomposite can be found in Appendix C to visualize how the electromagnetic waves interact with spherical particles.
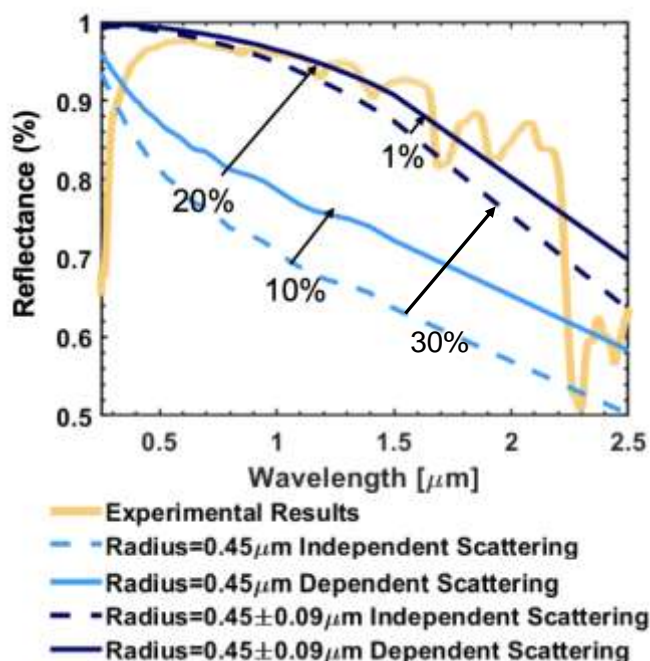
Figure 5.12 Reflection of CaCO₃ nanocomposite to study the effect of multiple particles sizes and dependent scattering

Table 5.5 Total reflection of CaCO₃ nanocomposite in solar range for both single and multiple particle sizes (R=0.45μm)

Model	Total Solar Reflectance [%]
Experimental (———)	95.1
Simulation (– –) R=0.45μm	74.2
Simulation (———) R=0.45μm	81.3
Simulation (– –) R=0.45 $\pm$ 0.09 μm	96.3
Simulation (———) R=0.45 $\pm$ 0.09 μm	96.8

From Table 5.5, it can be seen that after the application of the dependent scattering correction factor for multiple particle sizes, there is a significant 30% increase in total reflection compared to

the initial single particle case with 0.45μm particle radius. 15% in the UV, 24% in the VIS and 37% in the NIR (Table B.2). Due to the limitation of the acrylic properties, the NIR range fluctuation is not fully captured. As illustrated in Figure 5.13, the absorption of acrylic is plotted in green. Its absorption peaks correspond to the low reflection points from the experiments, which indicates that whenever acrylic absorbs the most, the reflection of the nanocomposite decreases the most. Therefore, in the future, when acrylic absorption can be implemented in the simulation, the model would achieve more robust results by capturing the absorption of the acrylic.
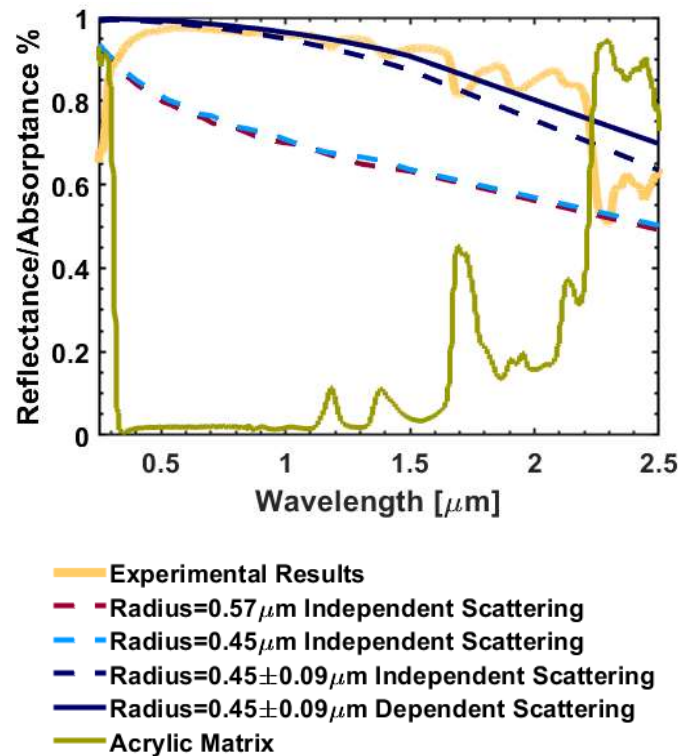
Figure 5.13 Reflection of CaCO₃ nanocomposite and absorption of acrylic matrix

6. CONCLUSION AND FUTURE DIRECTIONS

Motived by the challenges of radiative cooling applications and inspired by the promising properties of biomaterials, this work 1) measured the optical properties of the shells, 2) synthesized a coating that strengthen the characteristics of seashells using $CaCO_3$ to achieve desired cooling performance in high temperature operating conditions and 3) developed a tool with Mie theory and Monte Carlo Simulation to capture the reflectance of the nanocomposite for high volume concentration computationally. Compared to a single particle size $CaCO_3$, the total reflectance of multiple particle sizes with incorporated dependent scattering correction demonstrated a 30% increase, from 75% to 97%. In the UV range, the reflection increases from 86% to 99.6%. This bio-inspired nanocomposite not only provides a cost effective alternative for mass production, but also minimizes the absorption in the UV range found in most other non-metal radiative cooling materials. The total solar reflectance of the optimized multi-particle size $CaCO_3$ can achieve up to 97% and it is in excellent agreement the experimental results. Insights obtained from this study will aid researchers in selecting economical, scalable, and manufacturable materials for radiative cooling applications.

APPENDIX A. SEM IMAGES
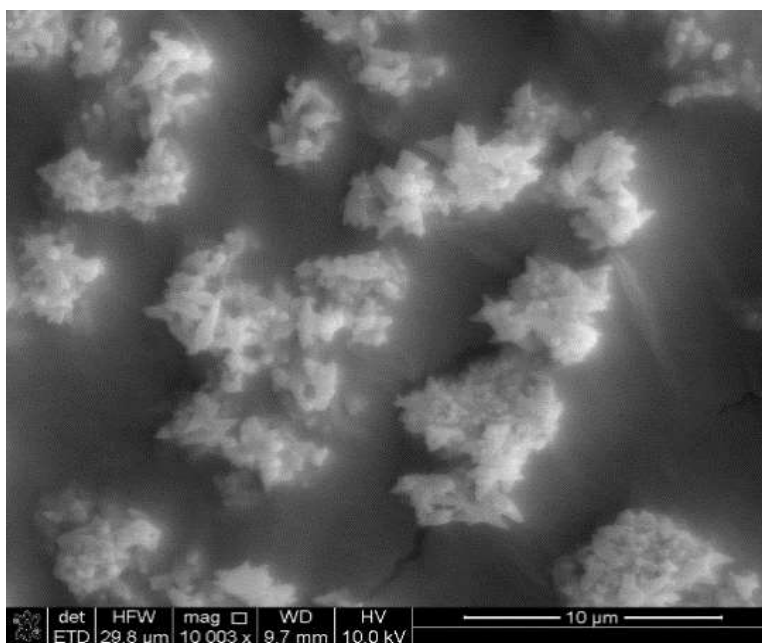
Figure A.1 SEM of CaCO$_3$ with 10 K Magnification
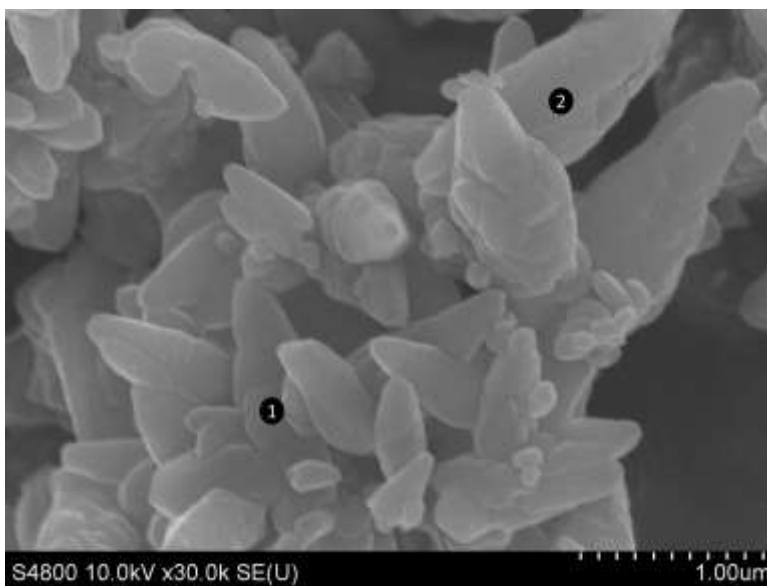
Figure A.2 SEM of CaCO$_3$ with 30K Magnification for sample 1 and 2
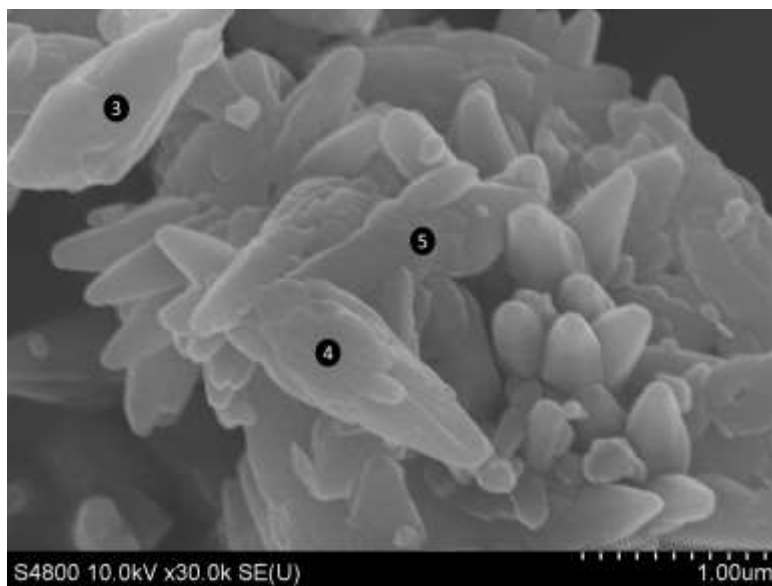
Figure A.3 SEM of CaCO$_3$ with 30K Magnification for sample 3, 4 and 5
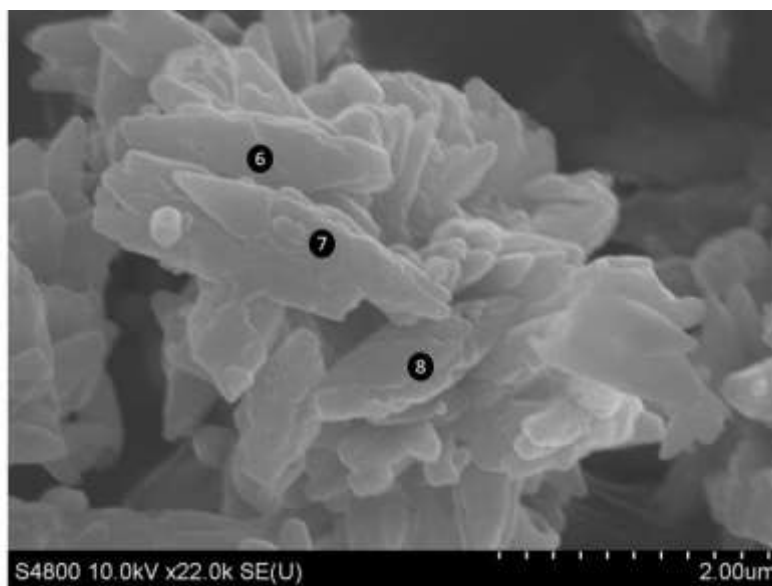
Figure A.4 SEM of CaCO$_3$ with 30K Magnification for sample 6, 7 and 8
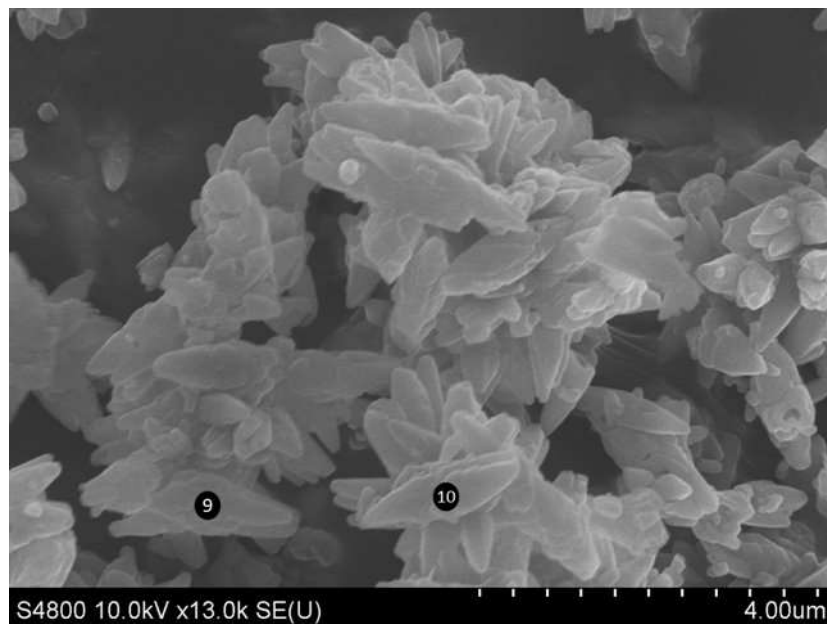
Figure A.5 SEM of CaCO₃ with 30K Magnification for sample 9 and 10

APPENDIX B. TABLES

Table B.1 Reflection in solar range for a single particle (R=0.57μm)

R=0.57μm	Single Particle
Total Reflection	73.3%
UV Reflection	85.9%
VIS Reflection	78.8%
NIR Reflection	68.8%

Table B.2 Reflection in solar range for single particle size, multiple particle size and after applying the dependent correction factor (R=0.45μm)

R=0.45μm	Single Particle Independent Scattering	Multi-Particle Independent Scattering	Multi-Particle Dependent Scattering
Total Reflection	0.743	0.963	0.968
UV Reflection	0.868	0.992	0.996
VIS Reflection	0.798	0.987	0.990
NIR Reflection	0.696	0.945	0.951

APPENDIX C. PHASE FUNCTION

When it comes to interactions between spheres and photons, there are three common categories for scattering: Rayleigh scattering, Mie scattering, and geometric scattering. If the diameter of a particle is comparable to the wavelength of the incoming light, then it is considered to be the Mie scattering. When the diameter of a particle is smaller than the wavelength of the incoming light, Rayleigh scattering will be observed. Geometric scattering is used when the diameter of the particle is a lot larger than the wavelength of the incoming light [40]. To predict and visualized the scattering trajectory of the particle photon interaction, the scattering phase function can be utilized. When the interaction falls into the Mie scattering region, a forward weighted scattering phase function will present. Rayleigh scattering refers to a relatively equivalent forward and backward scattering phase function. If particles and photons are interacting in the Geometric scattering region, then a forward scattering phase function will be generated [40]. Existing literatures have explored how to calculate the scattering phase function [37][50][34]. Deirmendjian [51] proposed a simplified approach to calculate direction-dependent functions and the scattering amplitudes, S_1 and S_2, leading to the visualization of the scattering phase function.

The scattering phase function characterizes the angular dependence of the scattered light. At each wavelength, the function informs us with the directional dependence of the scattering of the electromagnetic wave. In order to plot the phase function, the direction-dependent functions π_n and τ_n need to be calculated first as the following:

$$\pi_n(cos\theta) = \frac{dP_n(cos\theta)}{dcos(\theta)}$$

(C.1)

$$\tau_n(cos\theta) = cos\theta\,\pi_n(cos\theta) - sin^2\theta\,\frac{d\pi_n(cos\theta)}{dcos(\theta)}$$

(C.2)

where P_n is the corresponding Legendre polynomials. Equation C.3 and C.4 are developed from Equations C.1 and C.2 according the method proposed by Deirmendjian [51] where $0 \le \theta \le \pi$ and $\pi_0 = 0$, $\pi_1 = 1$, $\pi_2 = 3cos\theta$, $\tau_0 = 0$, $\tau_1 = \cos\theta$, and $\tau_2 = 3cos2\theta$

$$\pi_n(\theta) = cos\theta\,\frac{2n-1}{n-1}\,\pi_{n-1}(\theta) - \frac{n}{n-1}\pi_{n-2}(\theta)$$

(C.3)

$$\tau_n(\theta) = n\cos\theta\,\pi_n(\theta) - (n+1)\,\pi_{n-1}(\theta)$$

(C.4)

From π_n and τ_n, the scattering amplitudes, S_1 and S_2, can be calculated using Eq. C.5 and Eq. C.6.

$$S_1(\theta) = \sum_{n=1}^{\infty}\frac{(2n+1)}{n(n+1)}(a_n\pi_n + b_n\tau_n)$$

(C.5)

$$S_2(\theta) = \sum_{n=1}^{\infty}\frac{(2n+1)}{n(n+1)}(a_n\tau_n + b_n\pi_n)$$

(C.6)

The scattering phase function for a single particle size can be calculated based on Eq.C.7

$$\Phi_s(\theta) = 2\frac{|S_1|^2 + |S_2|^2}{x^2 Q_{sca}}$$

(C.7)

The scattering phase function for multiple particle sizes Eq. C.8 can be obtained from the single particle size phase function in Eq. C.7 [16], [40].:

$$\Phi_T(\theta) = \frac{1}{\sigma_T} \sum_{i=1}^{c} \frac{3f_i \Phi_{s,i}(r_i, \theta) Q_{sca,i}}{2d_i}$$

(C.8)
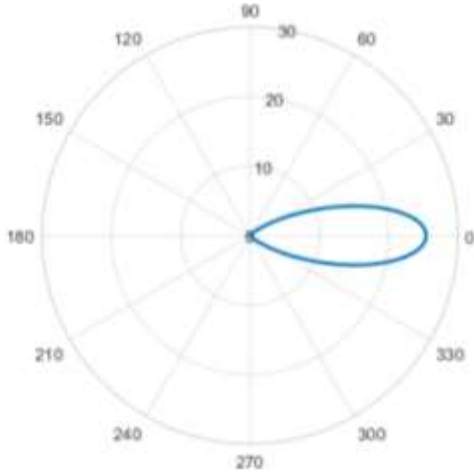
Figure C.1 Mie Scattering Phase Function for wavelength= $0.9\mu m$, radius =$0.4\mu m$
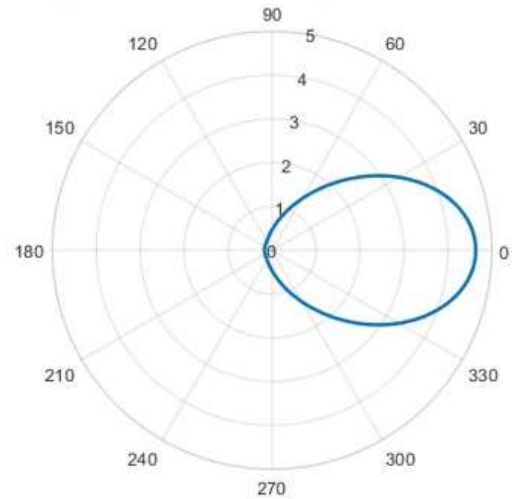
Figure C.2 Mie Scattering Phase Function for wavelength= $2.5\mu m$, radius =$0.4\mu m$
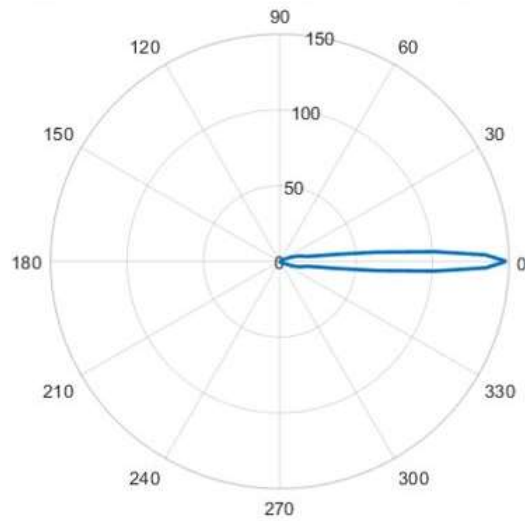
Figure C.3 Mie Scattering Phase Function for wavelength= $0.24\mu m$, radius =$0.4\mu m$

REFERENCES

[1]   "Energy Saver 101 Infographic: Home Cooling | Department of Energy." [Online]. Available: https://www.energy.gov/articles/energy-saver-101-infographic-home-cooling. [Accessed: 07-Apr-2019].

[2]   E. R. Switzer and M. R. Greason, "National Aeronautics and Space Administration Goddard Space Flight Center LAMBDA - Cosmic Background Explorer." [Online]. Available: https://lambda.gsfc.nasa.gov/product/cobe/. [Accessed: 18-Mar-2019].

[3]   A. Gentle, J. Aguilar, G. S.-S. E. M. and S. Cells, and undefined 2011, "Optimized cool roofs: Integrating albedo and thermal emittance with R-value," *Elsevier*.

[4]   A. R. Gentle and G. B. Smith, "Radiative Heat Pumping from the Earth Using Surface Phonon Resonant Nanoparticles," *Nano Lett.*, vol. 10, no. 2, pp. 373–379, Feb. 2010.

[5]   C. G. Granqvist and A. Hjortsberg, "Radiative cooling to low temperatures: General considerations and application to selectively emitting SiO films," *J. Appl. Phys.*, vol. 52, no. 6, pp. 4205–4220, Jun. 1981.

[6]   C. G. Granqvist and A. Hjortsberg, "Surfaces for radiative cooling: Silicon monoxide films on aluminum," *Appl. Phys. Lett.*, vol. 36, no. 2, pp. 139–141, Jan. 1980.

[7]   P. Berdahl, "Radiative cooling with MgO and/or LiF layers," *Appl. Opt.*, vol. 23, no. 3, p. 370, 2009.

[8]   P. Berdahl, M. Martin, and F. Sakkal, "Thermal performance of radiative cooling panels," *Int. J. Heat Mass Transf.*, vol. 26, no. 6, pp. 871–880, 2010.

[9]   B. Orel, M. Gunde, A. K.-S. Energy, and undefined 1993, "Radiative cooling efficiency of white pigmented paints," *Elsevier*.

[10]   S. N. David *et al.*, "Scalable-manufactured randomized glass-polymer hybrid metamaterial for daytime radiative cooling," *Science (80-.).*, vol. 355, no. 6329, pp. 1062–1066, Mar. 2017.

[11]   A. P. Raman, M. A. Anoma, L. Zhu, E. Rephaeli, and S. Fan, "Passive radiative cooling below ambient air temperature under direct sunlight," *Nature*, vol. 515, no. 7528, pp. 540–544, Nov. 2014.

[12]   E. Rephaeli, A. Raman, and S. Fan, "Ultrabroadband Photonic Structures To Achieve High-Performance Daytime Radiative Cooling," *Nano Lett.*, vol. 13, no. 4, pp. 1457–1461, Apr. 2013.

[13]   A. R. Gentle and G. B. Smith, "A Subambient Open Roof Surface under the Mid-Summer Sun," *Adv. Sci.*, vol. 2, no. 9, p. 1500119, Sep. 2015.

[14]   S. Atiganyanun *et al.*, "Effective Radiative Cooling by Paint-Format Microsphere-Based Photonic Random Media," vol. 18, p. 12, 2019.

[15]   J. Kou, Z. Jurado, Z. Chen, S. Fan, and A. J. Minnich, "Daytime Radiative Cooling Using Near-Black Infrared Emitters," *ACS Photonics*, vol. 4, no. 3, pp. 626–630, Mar. 2017.

[16]   Z. Huang and X. Ruan, "Nanoparticle embedded double-layer coating for daytime radiative cooling," *Int. J. Heat Mass Transf.*, vol. 104, pp. 890–896, Jan. 2017.

[17]   J. Peoples *et al.*, "A strategy of hierarchical particle sizes in nanoparticle composite for enhancing solar reflection," *Elsevier*.

[18]   G. Kiani, L. Olsson, … A. K.-I. T., and undefined 2011, "Cross-dipole bandpass frequency selective surface for energy-saving glass used in buildings," *ieeexplore.ieee.org*.

[19] H. Bao, C. Yan, B. Wang, X. Fang, C. Y. Zhao, and X. Ruan, "Double-layer nanoparticle-based coatings for efficient terrestrial radiative cooling," *Sol. Energy Mater. Sol. Cells*, vol. 168, pp. 78–84, Aug. 2017.

[20] A. W. Harrison and M. R. Walton, "Radiative cooling of TiO2 white paint," *Sol. Energy*, vol. 20, no. 2, pp. 185–188, Jan. 1978.

[21] A. Andretta, B. Bartoli, … B. C.-L. J., and undefined 1981, "Selective surfaces for natural cooling devices," *jphyscol.journaldephysique.org*.

[22] T. M. J. Nilsson and G. A. Niklasson, "Radiative cooling during the day: simulations and experiments on pigmented polyethylene cover foils," *Sol. Energy Mater. Sol. Cells*, vol. 37, no. 1, pp. 93–118, Apr. 1995.

[23] R. Levinson, P. Berdahl, H. A.-S. E. M. and S. Cells, and undefined 2005, "Solar spectral optical properties of pigments—Part II: survey of common colorants," *Elsevier*.

[24] K. Schmidt-Nielsen, C. R. Taylor, and A. Shkolnik, "Desert snails: problems of heat, water and food.," *J. Exp. Biol.*, vol. 55, no. 2, pp. 385–98, 1971.

[25] C. Woon, P. Shek, … M. T.-A. M. and, and undefined 2015, "Compressive strength of ground waste seashells in cement mortars for masonry and plastering," *Trans Tech Publ*.

[26] Y. Kim, S. H.-K. J. of E. Health, and undefined 2010, "The Utilization of Waste Seashell for High Temperature Desulfurization," *koreascience.or.kr*.

[27] X. Li, Z. Huang, J. Pepoples, Z. Zhao, J. Qiu, and X. Ruan, "Ultra-efficient Low-cost Radiative Cooling Paints," 2019.

[28] N. Berrahmouni and N. Burgess, "Northern Africa | Ecoregions | WWF." [Online]. Available: https://www.worldwildlife.org/ecoregions/pa1327. [Accessed: 26-Mar-2019].

[29] N. Shi, C. Tsai, F. Camino, G. Bernard, … N. Y.-, and undefined 2015, "Keeping cool: Enhanced optical reflection and radiative heat dissipation in Saharan silver ants," *science.sciencemag.org*.

[30] G. Swayze, R. Clark, … T. K.-B. of the, and undefined 1993, "The US Geological Survey, Digital Spectral Library: Version 1: 0.2 to 3.0 mum," *adsabs.harvard.edu*.

[31] G. Theses *et al.*, "An investigation of tio2-znfe2o4 nanocomposites for visible light photocatalysis Scholar Commons Citation An Investigation of TiO 2-ZnFe 2 O 4 Nanocomposites for Visible Light Photocatalysis," 2005.

[32] F. Hossain, G. Murch, I. Belova, B. T.-S. S. Communications, and undefined 2009, "Electronic, optical and bonding properties of $CaCO_3$ calcite," *Elsevier*.

[33] M. F. (Michael F. . Modest, *Radiative heat transfer*. Elsevier Science, 2013.

[34] C. Mätzler, "MATLAB Functions for Mie Scattering and Absorption," 2002.

[35] C. Tien, B. D.-A. R. of H. Transfer, and undefined 1987, "Thermal radiation in part1culate media with dependent and independent scattering," *dl.begellhouse.com*.

[36] T. Wriedt, "Mie Theory: A Review," 2012, pp. 53–71.

[37] C. Bohren and D. Huffman, *Absorption and scattering of light by small particles*. Wiley, 1983.

[38] H. Hulst and H. van de Hulst, *Light scattering by small particles*. 1981.

[39] M. Kerker, *The scattering of light and other electromagnetic radiation: physical chemistry: a series of monographs*. 2013.

[40] M. Michael F, "Radiative Heat Transfer," *Acad. Press*, 2003.

[41] L. Wang, S. Jacques, L. Z.-C. methods and programs in, and undefined 1995, "MCML—Monte Carlo modeling of light transport in multi-layered tissues," *Elsevier*.

[42] R. Vaillon, B. Wong, M. M.-S. and R. Transfer, and undefined 2004, "Polarized radiative transfer in a particle-laden semi-transparent medium via a vector Monte Carlo method," *Elsevier*.

[43] J. Howell, M. Menguc, and R. Siegel, *Thermal radiation heat transfer*. 2015.

[44] J. R. Frisvad, N. J. Christensen, and H. W. Jensen, "Computing the scattering properties of participating media using Lorenz-Mie theory," *ACM Trans. Graph.*, vol. 26, no. 3, p. 60, 2007.

[45] Ž. Ivezić and M. P. Mengüç, "An investigation of dependent/independent scattering regimes using a discrete dipole approximation," *Int. J. Heat Mass Transf.*, vol. 39, no. 4, pp. 811–822, Mar. 1996.

[46] M. Mishchenko, *Electromagnetic scattering by particles and particle groups: an introduction*. 2014.

[47] B. P. Singh and M. Kaviany, "Modelling radiative heat transfer in packed beds," *Int. J. Heat Mass Transf.*, vol. 35, no. 6, pp. 1397–1405, 1992.

[48] S. Redmond, S. C. Rand, X. L. Ruan, and M. Kaviany, "Multiple scattering and nonlinear thermal emission of Yb3+, Er3+:Y2O3 nanopowders," *J. Appl. Phys.*, vol. 95, no. 8, pp. 4069–4077, 2004.

[49] M. E. Reid, I. D. Hartley, and T. M. Todoruk, "Determination of true optical absorption and scattering coefficient of wooden cell wall substance by time-of-flight near infrared spectroscopy," *Trans. Terahertz. Sci*, vol. 2, no. 1, pp. 560–587, 2012.

[50] S. Chandrasekhar, *Radiative transfer*. 2013.

[51] D. Deirmendjian, "Electromagnetic Scattering on Spherical Polydispersions," 1969.

PUBLICATIONS

Zhao, V., Lopez, C. E., and Tucker, C. S, "*Evaluating the impact of idea dissemination methods on information loss*," in ASME Journal of Computing and Information Science in Engineering (2019)

Zhao V., Tucker CS. "*Categorization of Information Loss During the Dissemination of Design Ideas*," in ASME Int. Design Engineering Technical Conf. & Computer and Informatics Engineering. Conf. (2018)

Berdanier, C.G., Buswell, N.T. and **Zhao, Z.,** *"Data visualization for time-resolved real-time engineering writing processes."* in ASEE Annual Conference and Exposition, Conference Proceedings (2018).